



Deformation and regimes of liquid column during water exit of a partially submerged sphere using the front-tracking lattice Boltzmann method

Haohao Hao^{a,c,1}, Jianyang Yu^{a,1,*}, Yanping Song^{a,1}, Fu Chen^{a,1}, Tian Liu^{b,1}

^a School of Energy Science and Engineering, Harbin Institute of Technology, Harbin 150001, PR China

^b College of Shipbuilding Engineering, Harbin Engineering University, Harbin 150001, PR China

^c School of Engineering and Materials Science, Queen Mary University of London, London E1 4NS, UK

ARTICLE INFO

Article history:

Received 2 September 2019

Received in revised form 10 September 2020

Accepted 11 September 2020

Available online 1 October 2020

Keywords:

Water exit

Partially submerged sphere

Liquid column

Dynamic deformation

Regimes

Lattice Boltzmann method

ABSTRACT

When a solid sphere exits water at a given velocity, the liquid column is pulled out of a liquid reservoir. The present study focuses on the dynamic deformation of the liquid column and on the identification of the liquid column regime on the Weber number and dimensionless time ($We-t^*$) map. The three-dimensional model of water exit has been established on the basis of the lattice Boltzmann method. A mass tracking algorithm was incorporated to capture the free surface, where the liquid–gas two-phase flow is simplified to a single-phase free surface flow. The surface tension is included by adding a perturbation term and the gravity as a body force is introduced in form of calculating the equilibrium distribution with an altered velocity. The contact angle condition in numerical simulation is not considered. The accuracy of the numerical results is demonstrated through the comparisons with the prior numerical and the experimental results in the literature. A parametric study has been conducted numerically on the radius and volume and of liquid column. Besides, the relationship between the pinch-off time of a liquid column and the Froude number has been obtained. Moreover, the evolution of the liquid column shape with a wide range of the Weber number and time scales are discussed based on the number of ligaments and droplets. The liquid column exhibits different characteristics and has been divided into three regimes. The transition between different regimes has been analyzed and the critical Weber number is given.

© 2020 Elsevier Ltd. All rights reserved.

1. Introduction

Nonlinear dynamics and breakup of free-surface flows are classical problems (Eggers, 1997). Water exit of a body is an interesting example of such a flow and appears in many natural and industrial processes. For example, marine life breaches the free surface for various purposes and some animals use their tongue pulling a liquid column from bath (Kim and Bush, 2012). The important applications include missile exit (Wang et al., 2014), underwater vehicle exit (Guo et al., 2019; Hao et al., 2019; Tassin et al., 2013) and sea structures (Faltinsen, 1993). During the water exit stage, non-stationary free liquid bridge is generated. The shape and evolution of the liquid bridge are crucial and open questions with scientific interest due to the richness of the underlying physics.

* Corresponding author.

E-mail address: yujianyang@hit.edu.cn (J. Yu).

¹ The authors are not aware of any biases that might be perceived as affecting the objectivity of this paper.

Numerous experimental and computational studies have been carried out to investigate the nonlinear deformation of free-surface flow during the stage of a body penetrating through the free surface. Greenhow and Lin (1983) captured the surface elevations above the cylinder and an interesting form of breaking in their experiment, which was termed as “waterfall breaking” by peregrine. They pointed out that the vortices shed by the cylinder interact with the free surface to complicate the breaking, which may be caused by a pressure inversion across the free surface. More than two decades later, Zhu et al. (2006) performed a numerical study using the Constrained Interpolation Profile method and got a conclusion similar to Greenhow and Lin (1983). Recently, a thorough assessment of the dynamics of both oblique and asymmetric water entry has been provided by Russo et al. (2018a) and the hydrodynamics of the interaction of the buoyant cylinders with the water free surface upon impact is analyzed through experimental measurements (Russo et al., 2018b).

Liju et al. (2001) performed the experiment and numerical simulation to study the deformation of the free surface before it breaking during the water exit of an axisymmetric body for the Froude number in the range $0.32 < Fr < 2.7$ and Weber number (We) in the range $0.7 < We < 89$. Rajavaheinthan and Greenhow (2015) used the BEM (Boundary Element Method) with the fully-nonlinear boundary conditions to investigate the free surface deformation, pressure and force for the water exit of 2D partially submerged bodies with constant accelerations. Subsequently, Ni et al. (2015) presented an analysis of the step-by-step free surface deformation using BEM for different Froude numbers ($Fr=0.3$ and 1) and the body shapes during the water exit of a fully-submerged rigid body. The free-surface profiles before and after detachment from the body were given for the whole water exit. Later, the free surface deformation and its dynamic change during the water exit of a sphere for Fr less than 1.24 , such as its spike, detachment and breakup, were studied by means of the experiment by Wu et al. (2017).

Similar to the large deformation of the free surface pulled by a cylinder or a sphere mentioned above, the stretching and break-up of liquid bridges have attracted much attention for different geometrical configuration, such as the circular tube and the flat plate. Marmottant and Villermaux (2004a) studied liquid ligaments produced by the withdrawal of a tube initially dipping at a free surface. They investigated the stretching and fragmentation of liquid ligaments at small and large extension rates. Furthermore, the experiments about the liquid column formation pulled by an upward rounded rod was carried out by Gart et al. (2015), which helps to explain how dogs exploit the fluid dynamics of the generated column.

Similarly, Reis et al. (2010) performed a series of experiments in which a glass disk, initially placed on a water surface, was pulled vertically upward to examine how cats lap and help understand the mechanism of lapping. Tassin et al. (2017) investigated experimentally the time evolution of the wetted surface during the lifting of a flat plate initially floating at the water surface using LED edge lighting technique and captured a contact line with a time-evolving complex shape of the free surface. Champougny et al. (2017) studied the break-up of free films pulled out of a pure liquid bath and derived a lubrication model to describe the non-stationary free liquid film. Besides, the stretching and breakup of a Newtonian liquid bridge between two plates are studied using numerical computation and experiment (Dodds et al., 2009, 2012; Doshi et al., 2003; Weickgenannt et al., 2015).

Past research has shown the nonlinear deformation of the free surface (spike, pinch-off, fragmentation and breakup) during water exit of a body for different scales depends on many factors, such as acceleration, Reynolds number, Froude number and Weber number. Kim et al. (2018) studied a liquid column extended by a solid sphere rising with constant acceleration from a liquid bath and proved the pinch-off location depending significantly on the acceleration of the solid sphere. Moreover, Reis et al. (2010) investigated the effect of Froude number to the pinch-off of the liquid column. Gart et al. (2015) argued that viscous and capillary forces should be negligible compared with inertia and gravity at high Reynolds (10^3 – 10^4), Froude (10^0 – 10^1), and Weber (10^1 – 10^3) through dimensional analysis. Wu et al. (2017) showed that as the Froude number increases under it ranging from 0.16 to 0.58 , the time to pinch-off of the free surface decreases, whereas its height increases for the water exit of a partially-submerged sphere. Liju et al. (2001) found that for Re less than about 200 , it has an obvious effect on the interface elevation of the spike.

Additionally, the Weber number plays a key role in breakup of liquid bridge pulled by a body, which is nearly identical to the jet breakup (Amirshaghghi et al., 2018; Jarrahbashi et al., 2016; Zhang et al., 1996). For further reviews of fragmentation of this problem, we refer the reader to the papers of Eggers (1997), Villermaux (2007) and Eggers and Villermaux (2008).

A review of the literature shows most of the studies on the water exit of a partially submerged object (sphere, circular tube and flat plate) were confined to the cases at small characteristic scale (e.g. capillary length $l_c = \sqrt{\sigma/\rho_l g}$, where σ is the surface tension, ρ_l is the liquid density and g is the gravitational acceleration.) or low Froude number Fr , Weber number We and Reynolds number Re , which means that the surface tension, capillary forces and viscous force are dominant with respect to the gravity and inertial force.

However, some aquatic and semi-aquatic animals with centimeter or decimeter scales jump out of water to escape from predators, breathe or capture prey (Chang et al., 2019). Chen et al. (2017) designed the hybrid aerial–aquatic robot with centimeter scale and their inspiration came from several animal species which exhibit multimodal locomotive capabilities in aerial and aquatic environments. There are some key technology for this robot. For example, when the robot exits water, it carries a large volume of fluid that is referred to as an entrained mass, which has a significant influence on the performance of the hybrid aerial–aquatic robot. Therefore, the studies on characteristics of the nonlinear deformation of the free surface in moderate Froude number and high Weber number region help understand the jumping dynamics of a variety of aquatic and semi-aquatic animals and establish foundation for the water-exiting robot.

In this paper, the dynamic deformation and regimes of the liquid column generated by the water exit of a partially submerged sphere are investigated using a front-tracking lattice Boltzmann approach (Thurey, 2007). The Froude number (Fr) and Weber number (We) ranging between 0.16–8.24 and 520–210,000 respectively are chosen by referring to the characteristic scales of the aquatic animal and hybrid aerial–aquatic robot. The main objective of this work is to investigate the nonlinear deformation of the free surface for the water exit of a partially submerged sphere and provide more physical insights of the flow which has not been discussed in the previous experimental and numerical studies.

The rest of this paper is organized as follows. In Section 2, the numerical methods will be given. In Section 3, the numerical model is validated. In Section 4, the dynamic deformation of the liquid column before its breakup is discussed. The liquid column regimes and its transition are presented in Section 5. Finally, some conclusions are obtained in Section 6.

2. Numerical methods

The lattice Boltzmann method (LBM) is a parallel and efficient algorithm for simulating multiphase fluid flows (Chen and Doolen, 1998). In addition, it is especially useful for modeling complicated boundary conditions and capturing motion of interfaces. This method has been demonstrated to deal with the issues involving the nonlinear deformation of free surface flow and breakup of droplets (Biscarini et al., 2013; Kékesi et al., 2014; Komrakova et al., 2014; Mitchell et al., 2018; Zarghami et al., 2014). Therefore, this method is used to simulate the dynamic deformation of liquid column pulled out by an object in liquid pool.

2.1. Lattice-Boltzmann equations

The common Lattice-Boltzmann equation has the following form (Chen et al., 1991)

$$f_i(x + c_i dt, t + dt) - f_i(x, t) = \Omega_i \quad (1)$$

where f_i , i , c_i and Ω_i denote the distribution functions, the direction of distribution functions, the lattice velocity and the collision operator, respectively.

A single-relaxation time (SRT) based on the Bhatnagar–Gross–Krook (BGK) approximation (Chen et al., 1991; Qian et al., 1992) is used and given by

$$\Omega_i^{BGK} = \frac{1}{\tau}(f_i^{eq} - f_i) \quad (2)$$

where f_i^{eq} is the local equilibrium function towards which the state is relaxed. The parameter τ in Eq. (2) is the relaxation time, which controls the lattice kinematic fluid viscosity through the relation (Benzi et al., 1992), as follows

$$v = c_s^2(\tau - \frac{1}{2}) \quad (3)$$

where c_s is the lattice sound speed.

The macroscopic quantities are calculated by taking the moment of the $f_i(x, t)$ and pressure is from the state equation, as follows

$$\begin{cases} \rho(x, t) = \sum_i f_i(x, t) \\ \rho u(x, t) = \sum_i c_i f_i(x, t) \\ p = \rho(x, t) c_s^2 \end{cases} \quad (4)$$

where c_i is one of a small discrete set of velocities $\{c_i\}$. ρ is the fluid density and u is the fluid velocity.

Herein, we use the D3Q19 model, where D3 is the space dimension of the simulation and Q19 refers to the number of discrete velocities (i.e. $\{i = 0, \dots, 18\}$), as shown in Fig. 1. To discretize the Maxwell distribution, an equilibrium distribution function for the single-phase collision operator proposed by Qian et al. (1992) is used and given by

$$f_i^{eq} = \rho w_i [1 + \frac{\mathbf{c}_i \bullet \mathbf{u}}{c_s^2} + \frac{(\mathbf{c}_i \bullet \mathbf{u})^2}{2c_s^4} - \frac{u^2}{2c_s^2}] \quad (5)$$

where $c_s = 1/\sqrt{3}$ and w_i are weighting parameters, as follows

$$w_i = \begin{cases} 1/3 & i = 0, \\ 1/18 & i = 1, 2, \dots, 6, \\ 1/36 & i = 7, 8, \dots, 18 \end{cases} \quad (6)$$

The distribution functions move on a D3Q19 lattice with the lattice velocity \mathbf{c}_i defined as

$$\mathbf{c}_i = (c_{ix}, c_{iy}, c_{iz}) = \begin{cases} (0, 0, 0)c, & i = 0, \\ (\pm 1, 0, 0)c, (0, \pm 1, 0)c, (0, 0, \pm 1)c, & i = 1, 2, \dots, 6, \\ (\pm 1, \pm 1, 0)c, (0, \pm 1, \pm 1)c, (\pm 1, 0, \pm 1)c & i = 7, 8, \dots, 18 \end{cases} \quad (7)$$

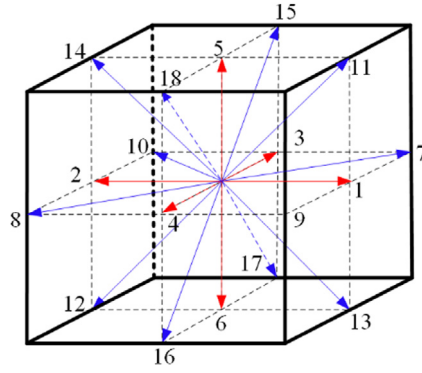
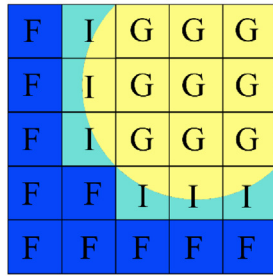
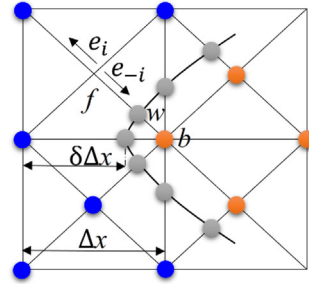


Fig. 1. D3Q19 velocity sets.



(a) Schematic of the free surface with fluid (F), interface (I) and gas.



(b) Sketch of the bounce-back boundary condition for the moving wall.

Fig. 2. Schematic of free surface and moving wall boundary.

where $c=dx/dt$, dx is the lattice spacing and dt is the time step. Both are normalized by the condition $dx/dt=1$.

The gravity is introduced by calculating the equilibrium distribution with an altered velocity (Buick and Greated, 2000), and defined as:

$$f_i^{eq} = \rho w_i \left[1 + \frac{\mathbf{c}_i \cdot \mathbf{u}^*}{c_s^2} + \frac{(\mathbf{c}_i \cdot \mathbf{u}^*)^2}{2c_s^4} - \frac{\mathbf{u}^* \cdot \mathbf{u}^*}{2c_s^2} \right] \quad (8)$$

where \mathbf{u}^* is the equilibrium velocity defined as

$$\mathbf{u}^* = \mathbf{u} + \mathbf{g}dt/2 \quad (9)$$

2.2. Free surface and moving wall boundary conditions

In this paper, the single phase free-surface model proposed by Körner et al. (2005) is used to solve the high density ratio problem, such as the jet breakup (Falcucci et al., 2010) and the buoyancy body interaction with the free surface (Facci et al., 2019).

The main advantages of this method are the neglect of the gas phase and the computational efficiency.

The lattice is divided into three types of cells (gas, interface and fluid cells), through the volume fraction of the fluid ε , as shown in Fig. 2(a). The fluid fraction is computed with the cell mass and density $\varepsilon = m/\rho$, where m is the fluid mass contained in the cell. The fluid fraction is equal to 0 and 1 for the gas and fluid cells, respectively. The fluid fraction varies from 0 to 1, which indicates cells are partially filled with fluid. The computation includes the following three steps (Falcucci et al., 2011):

The first step is determining the interface motion. For the mass exchange between two interface cells, their fluid fraction is considered to approximate the area they share at the cell boundary. For a cell located at x at time t , the mass

change due to the streaming of the i th population is given in the following Eqs. (10)–(11).

$$\Delta m_i(x, t) = \begin{cases} 0 & \forall (x + c_i dt) \in G \\ f_i^{pc}(x + c_i dt, t) - f_{-i}^{pc}(x, t) & \forall (x + c_i dt) \in F \\ (f_i^{pc}(x + c_i dt, t) - f_{-i}^{pc}(x, t)) * ((\varepsilon(x, t) + \varepsilon(x + c_i dt, t))/2) & \forall (x + c_i dt) \in I \end{cases} \quad (10)$$

$$m(x, t + \Delta t) = m(x, t) + \sum_{i=0}^{18} \Delta m_i(x, t) \quad (11)$$

where pc characterizes the post-collision state and $-i$ defines the opposite direction with respect to i . G , F and I represent, respectively, gas, fluid and interface cells.

The second step is determining the boundary conditions at the interface between gas and liquid. The distribution functions in interface cells coming from the direction of an empty cell during streaming must be reconstructed to ensure correct interface movement (Körner et al., 2005). Here, for an interface cell at site (x) with an empty cell at $(x + c_i dt)$, the post-streaming density function is governed by

$$f_{-i}^{pc}(x, t + dt) = f_i^{eq}(\rho_{gas}, u) + f_{-i}^{eq}(\rho_{gas}, u) - f_i(x, t) \quad (12)$$

where u is the fluid velocity at the interface cell.

The surface tension model introduced by Xing et al. (2007) is used to study the effect of the Weber number on the deformation of the liquid column, as given in the following Eqs. (13)–(14).

$$f_{-i}^{pc}(x, t + dt) = f_i^{eq}(\rho_{gas}, u) + f_{-i}^{eq}(\rho_{gas}, u) - f_i(x, t) + \Delta f_i \quad (13)$$

The surface tension is included by adding a perturbation term Δf_i , which is defined as

$$\Delta f_i = \beta |\partial m / \partial n| \cos 2(\theta_i - \theta_n) \quad (14)$$

where β is a constant chosen to set the surface tension for the model and the dependence of surface tension on β is basically linear (Gunstensen et al., 1991); $\partial m / \partial n$ is the mass gradient of the liquid whose direction is perpendicular to the interface; θ_i is the angle of the lattice direction i ; $\theta_n = \tan^{-1}(\frac{\partial m}{\partial y} / \frac{\partial m}{\partial x})$ is the angle of the local mass gradient. More details of the surface tension model can be found in Xing et al. (2007).

The last step is determining the cell-type updating. After the collision, the density is calculated to check whether the interface cell is to be filled or emptied during the time step, which can be expressed as

$$\begin{aligned} m(x, t + dt) &> (1 + \ell)\rho(x, t + dt) \rightarrow \text{cell filled,} \\ m(x, t + dt) &< (0 - \ell)\rho(x, t + dt) \rightarrow \text{cell emptied} \end{aligned} \quad (15)$$

where ℓ is an offset, usually $\ell = 10^{-3}$, which is used to prevent the new surrounding interface cells from being re-converted in the following LB step.

The above is only a brief introduction to this method. For a complete view on the accuracy of the method and the stability of the free interface involved, we refer the reader to the papers of Thurey (2007) and Falcucci et al. (2011).

We use the employed bounce-back boundary conditions to model a moving sphere. The schematic depiction of this boundary is shown in Fig. 2(b). Here, Δx denotes the space between lattice nodes. The subscripts b and f denote the lattice nodes on the body and fluid side, respectively, and w denotes the intersections of body's perimeter. The length fraction of the intersected link between x_f and x_b is $\delta = \|x_f - x_w\| / \|x_f - x_b\|$. The unknown probability density function on the sphere side is recovered as follows (Filippova and Hänel, 1997)

$$f_{-i}^{pc}(x_b, t) = (1 - \chi)f_i(x_f, t) + \chi f_i^*(x_b, t) + 2\omega_i \rho(x_b, t)[\mathbf{c}_i \bullet \mathbf{u}(x_w, t)] / c_s^2 \quad (16)$$

where $\mathbf{u}(x_w, t)$ is the boundary velocity at the intersection between the body and the link and χ is a weighting factor (Mei et al., 2000) defined as:

$$\chi = \begin{cases} (2\delta - 1)/(\tau + 1/2), & \delta \geq 0.5 \\ (2\delta - 1)/(\tau - 2), & \delta < 0.5 \end{cases} \quad (17)$$

here, u_{bf} and $f_i^*(x_b, t)$ is defined as (Mei et al., 2002)

$$\begin{aligned} \mathbf{u}_{bf} &= [(2\delta - 3)\mathbf{u}(x_f, t) + 3\mathbf{u}(x_w, t)] / 2\delta, & \delta \geq 0.5 \\ \mathbf{u}_{bf} &= [\mathbf{u}(x_f + c_{-i}, t)], & \delta < 0.5 \end{aligned} \quad (18)$$

$$f_i^*(x_b, t) = \omega_i \rho \left[1 + \frac{\mathbf{c}_i \bullet \mathbf{u}_{bf}}{c_s^2} + \frac{[\mathbf{c}_i \bullet \mathbf{u}(x_f, t)]^2}{2c_s^4} - \frac{\|\mathbf{u}(x_f, t)\|^2}{2c_s^2} \right] \quad (19)$$

The Mach numbers are $Ma = V_{max}/c_s < 1$ to guarantee sufficiently low compressibility effects and avoid the generation of non-physical reflection waves in the domain (Krüger et al., 2016), where V_{max} is the maximum lattice speed in all simulations. Moreover, for the computational domain boundary condition, the called fullway bounce-back method is used to satisfy the no-slip boundaries (Sukop and Thorne Jr, 2006).

2.3. Turbulence model

The LBM for high Reynolds number flows, without modeling unresolved small-scale effects on large scale dynamics, leads to numerical instabilities (Hou et al., 1994) because the numerical stability of LBM is limited once the relaxation parameter τ approaches 1/2 (which is equivalent to ω being close to 2). Therefore, we use the Wall-Adapting Local Eddy (WALE) viscosity model proposed by Ducros et al. (1998) to improve numerical stability and capture turbulent structures in the flow. In the filtered LB equation, the effect of the unresolved scale motion is modeled through the modified collision relaxation time τ_s ($\tau_s = 3(v + v_t) + 0.5$). The kinematic viscosity ν is reported in Eq. (3) and the eddy viscosity ν_t is formulated as follows

$$\nu_t = \Delta_f^2 \frac{(S_{\alpha\beta}^d S_{\alpha\beta}^d)^{3/2}}{(S_{\alpha\beta} S_{\alpha\beta})^{5/2} + (S_{\alpha\beta}^d S_{\alpha\beta}^d)^{5/4}} \quad (20)$$

where $\Delta_f = C_w dx$ is the filter scale, the constant C_w is 0.325 for all simulations in this paper and S is the strain rate tensor of the resolved scales computed as

$$S_{\alpha\beta} = \frac{g_{\alpha\beta} + g_{\beta\alpha}}{2} \quad (21)$$

$$S_{\alpha\beta}^d = \frac{1}{2} (g_{\alpha\beta}^2 + g_{\beta\alpha}^2) - \frac{1}{3} \delta_{\alpha\beta} g_{\gamma\gamma}^2 \quad (22)$$

where $g_{\alpha\beta}$ is equal to $\partial u_\alpha / \partial x_\beta$.

3. Validation with experiments

As described in this section, the applicability of the above algorithm to model water exit for a body was demonstrated. We have carried out the simulation of water exit of a partially submerged sphere at constant speeds ($V = 0.2, 0.5$ and 0.7 m/s) in previous study (Guo et al., 2019; Hao et al., 2019). It was compared against experimental measurements from water flume. Herein, other validation is performed in the case of the three-dimensional water exit of a partially submerged circular cone with constant vertical velocity. The numerical results are compared with those obtained by Song et al. (2019).

In order to make sure that the numerical simulation results are independent of the domain size, the computational domain should be sufficiently large in all three directions. The dimensions of the computational domain are 3 m in x direction, 3 m in y direction and 3 m in z direction, respectively. The water depth is 1.5 m. The height of the circular cone is $L = 0.2$ m and the cone angle is $\beta = 90$. The cone velocity is $V = 0.7$ m/s. The initial submergence of the bottom of the cone is 0.166 m. The dynamic viscosity and surface tension equal 1×10^{-3} Pa*s and 7.2×10^{-2} N/m, respectively. The gravitational acceleration is $g = 9.8$ m/s². Hence, the corresponding Reynolds number and Froude number are equal to 1.4×10^5 and 0.5, respectively. Note that $t = 0$ corresponds to the moment when the bottom of the cone attains the initial height of the free surface.

On the basis of the grid convergence in previous study (Guo et al., 2019), the lattice size and the time step for all the simulations are $L/\Delta x = 60$ and $\Delta t = 2 \times 10^{-5}$ s, respectively. Considering the axially symmetric flow for the water exit of the cone and phenomenon of the bubble entrapment, we show the temporal evolution of liquid column in the middle vertical plane in Fig. 3, which is compared against the experimental data of Song et al. (2019). Overall, the numerical predictions for the deformation of the free surface shown turn out to be in quantitative agreement with experimental measurements obtained by Song et al. (2019).

4. Dynamic deformation of liquid column without breakup

Inertial entrainment draws liquid upward into a column as a sphere rises vertically from the free surface. Ultimately, gravity prevails and the column pinches off. Evidently, the inertial force and gravity play a leading role in the motion of liquid column, compared with the viscous, capillary forces and surface tension (Gart et al., 2015; Reis et al., 2010). Therefore, the dynamic deformation of liquid column is dominated by the inertial force and gravity. The breakup of liquid column occurs when the value of the Weber number is increased up to the critical value, as discussed systemically in Section 5. The value of the Weber number is in this section below this critical value, which means the liquid column does not break up during its evolution. To understand this dynamic deformation, we analyze the temporal and spatial evolution of liquid column and the effect of the Froude number varying from 0.16 to 8.24 on the volume and pinch-off of liquid column.

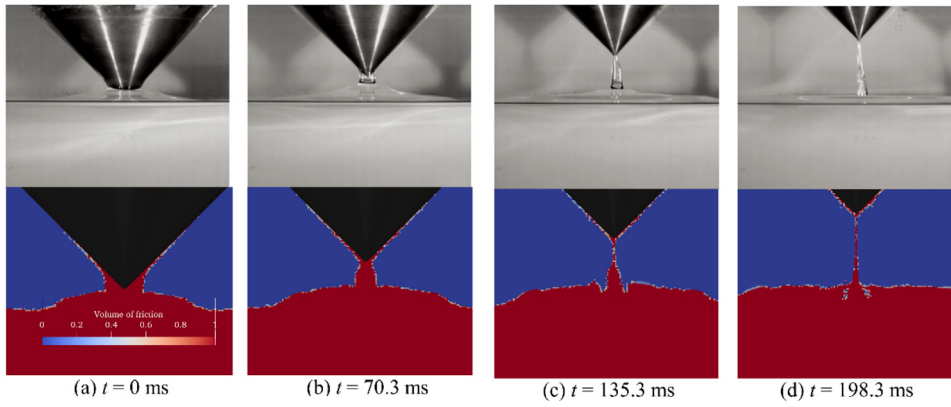


Fig. 3. Comparison of deformation of free surface disturbed by a circular cone at constant speed $V = 0.7$ m/s between experimental and numerical results.

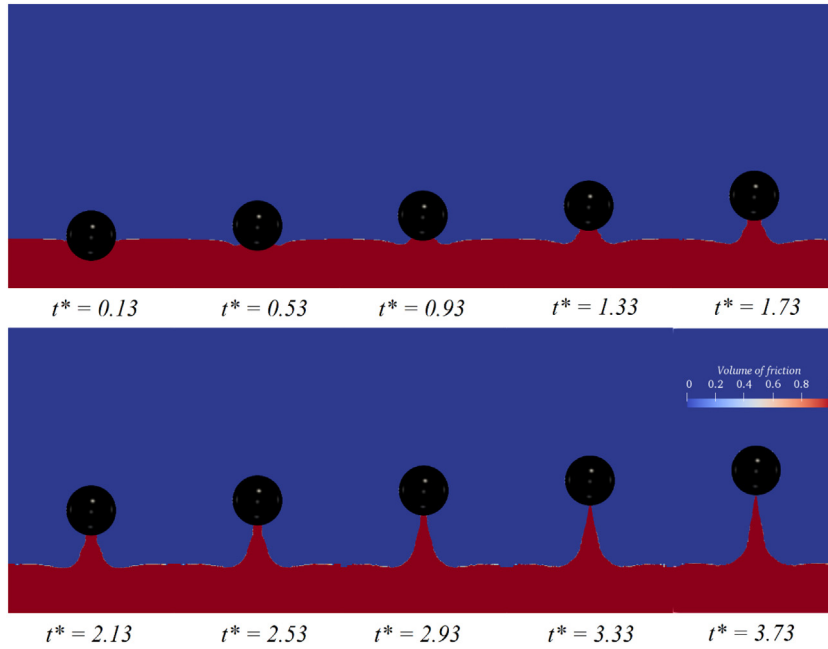


Fig. 4. Temporal evolution of liquid column in the middle vertical plane before pinch-off with the sphere rising vertically upwards with a Froude number of 1.65. The dark blue and the dark red represents air and water, respectively. (For interpretation of the references to colour in this figure legend, the reader is referred to the web version of this article.)

To generalize our numerical results, we normalize relevant variables using the sphere radius R as the characteristic length scale of the system and the sphere velocity V_c as the characteristic velocity scale. Thus, the corresponding characteristic time scale is $t_c = R/V$. The dimensionless time is $t^* = t/t_c$. $t^* = 0$ is the time when the center of sphere is level with the initial surface of clam water. The dimensionless volume of liquid is $V_{lc} = v_{lc}/\pi R^3$, where the v_{lc} are the volume of liquid column. The dimensionless radius and height of cross section of liquid column are $R_{lc} = r_{lc}/R$ and $H_{lc} = h_{lc}/R$, where the r_{lc} and h_{lc} are the radius and height of cross section of liquid column. The governing dimensionless groups are (1) the Froude number $Fr = V/\sqrt{gR}$, (2) the Reynolds number $Re = VR/\nu$, (3) the Weber number $We = 2\rho_l V^2 R/\sigma$, where ν and σ are the kinematic viscosity coefficient and the surface tension of the liquid, respectively. Except for the Froude number, almost all parameters, including diameter D , mass M , equivalent density ρ_s and initial submergence depth of the center of sphere H_i , are the same as those in the experiment by Wu et al. (2017). Note that the surface roughness of a sphere has been neglected in numerical simulation.

Fig. 4 shows the evolution of liquid column profiles with a Froude number of 1.65. As shown in this figure, the liquid column extends vertically upwards under the action of inertial force and gravity. Then it contracts radially inwards as the sphere ascends. From $t^* = 1.33$ to 1.73, the radius of liquid column decreases linearly as the height of its cross section

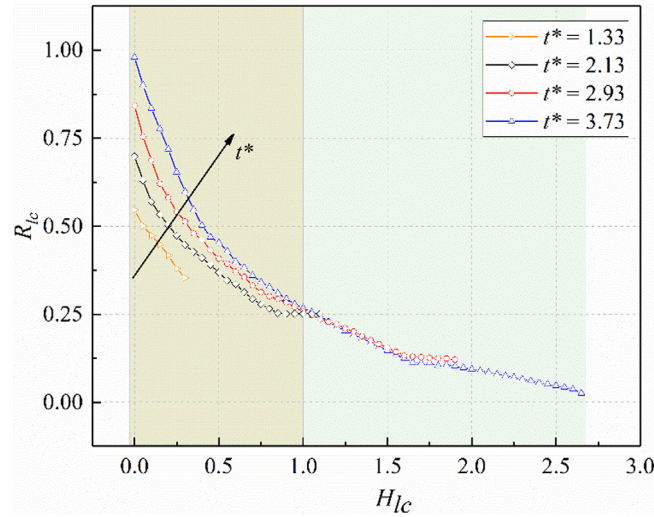


Fig. 5. Temporal evolution of the radius at the height of cross section of liquid column with a Froude number of 1.65.

increases, as also shown in Fig. 5. From $t^* = 1.73$ to 2.53, the upper portion of liquid column contracts dramatically as the rising continues. At $t^* = 3.73$, the liquid column pinches off from the sphere. Additionally, at this moment when the inertia effect is significant, the liquid column shape exhibits a cone-like structure. Similarly, Zhuang and Ju (2015) also found the liquid bridge shape under coaxial stretching appear a cone-like structure at higher stretching velocities. The gravitational force was not considered because the liquid bridges they studied is microscale. The entire deformation process is strikingly similar to the experimental results (Gart et al., 2015; Marmottant and Villermaux, 2004a; Reis et al., 2010; Tassin et al., 2017), although the shape of a body exiting the water is quite different from each other.

Fig. 5 shows the temporal evolution of the radius at the height of cross section of liquid column with a Froude number of 1.65. We can find that the liquid column has an evolution over time. Its radius R_{lc} at different heights has a remarkably increase when the height H_{lc} is less than 1.0, whereas, the radius of liquid column begins to decrease slightly when the height H_{lc} is greater than 1.0, especially for $t^* = 2.93$ and $t^* = 3.73$. To explain this phenomenon, the temporal and spatial evolution of radial velocity V_r' at heights $H_{lc} = 0$ and 1.75 are examined, as shown in Fig. 6. At $H_{lc} = 0$, the direction of the radial velocity V_r' is identical to the direction of the extension of the liquid column on its bottom. The radial velocity continually decreases as the sphere rises, which means the extension of the liquid column becomes more and more slowly. At $H_{lc} = 1.75$, the direction of the radial velocity V_r' is diametrically opposite to the direction of the extension of the liquid column on its top and the contracting velocity is considerably less than the expanding velocity.

Fig. 7 shows the temporal evolution of liquid volume pulled out of a liquid pool with different Froude numbers. The dimensionless liquid column volume dramatically decreases as the Froude number increases. The liquid volume consists of two parts, as shown in Fig. 8. The first part is the volume of liquid column that connects to the sphere. The second part is the volume of the bulge near the free surface and accounts for a large percentage of liquid volume. When the t^* equals each other for the different Froude numbers, the absolute time t for the low Froude number is greater than that for the high Froude number. This result in the larger volume of the bulge for the low Froude. Therefore, there is a negative correlation between the liquid volume and the Froude number. Besides, for $Fr = 0.41$, there exists the decrease in the liquid volume due to the liquid column and bulge descending before pinch off.

As mentioned above, the pinch off of liquid column ultimately occurs due to it continually contracting as a sphere forcedly ascends. We examine the pinch-off time of liquid column. The results for the pinch-off times t_{pc}^{**} versus the Froude number are shown in Fig. 9. The pinch-off time t_{pc}^{**} is as a function of Froude number and increases as Fr increases. Moreover, we can obtain the power law $t_{pc}^{**} \sim Fr^{2/3}$ from the numerical results and the experimental results of Wu et al. (2017) for the pinch-off time and Froude number, as shown in Fig. 9.

5. Liquid column regimes and its transition

As previously noted, the formation of the liquid column occurs during water exit of a partially submerged sphere due to the fluid inertia. The open literature shows that the liquid column pulled by an object is regular and systematic during ascent at low Weber number. However, the appearance of the liquid column with higher Weber number remains under explored. Besides, there are some similarities between the evolution of the shape of jet (Sallam et al., 2002) and the liquid column. For example, the Weber number and time scale play significant roles in the deformation of liquid involving its breakup and the formation of droplets. Thus, the liquid column regimes and the mechanisms responsible for the formation of regime will be investigated systematically for different Weber numbers and time scales.

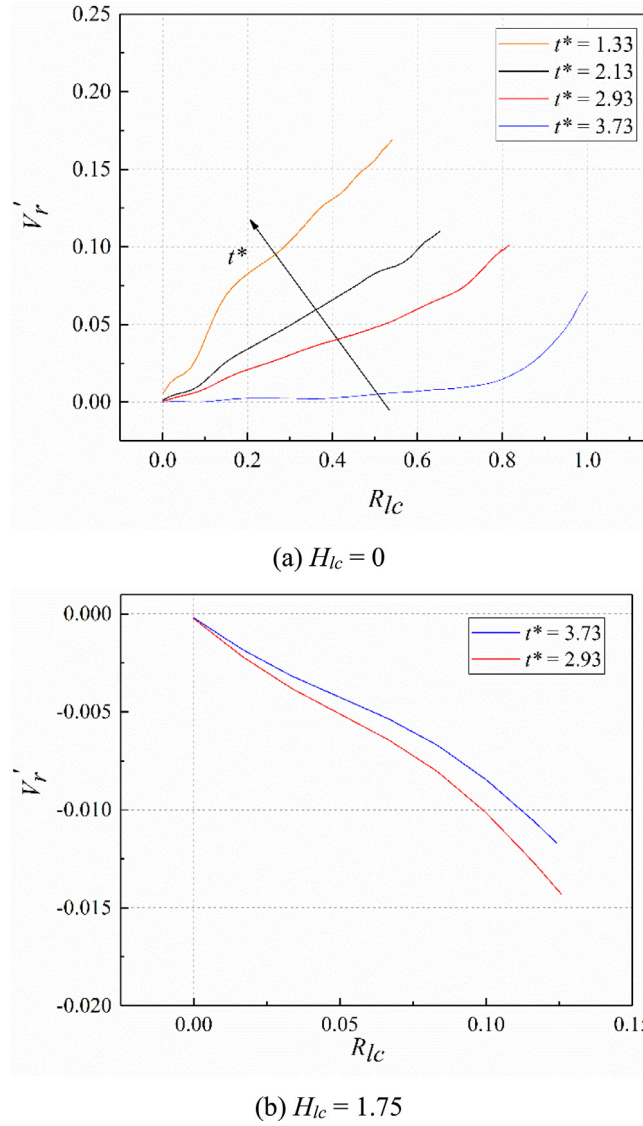


Fig. 6. Temporal and spatial evolution of the horizontal velocity at different heights.

5.1. Liquid column regimes

We summarize our findings in Fig. 10. The regime CR represents the regular liquid column. The regime UG signifies the unstable growth of the liquid column. The regime BU denotes the breakup of liquid column. The three liquid column regimes are classified by the number of ligaments and droplets N_d at different Weber numbers and time scales. Two filters of the Paraview are used to obtain N_d , namely the threshold and connectivity. The first is to generate the ligaments and droplets, and the other is to obtain its number. Fig. 11 shows an example of time history of the number of ligaments and droplets with a Weber number of 75,000. In this figure, there are two dramatic changes in the gradient of the number of ligaments and droplets. These phenomena occur at $t^* = 1.2$ and 4.4 , respectively, which are defined as the critical value to distinguish the different regimes for this Weber number. The specific characteristics of each regime and the mechanism of its formation are given in the following.

(a) Regime CR (Continuity and Regularity)

When the partially submerged sphere exits the free surface at a low velocity, it can be seen in Fig. 10(a) that the shape of the liquid column appears continuous and regular during its stretching. Therefore, this liquid column regime is defined as CR (Continuity and Regularity). Also, the liquid column diameter is as a function of the height. The non-equal diameter liquid cylinder becomes thinner and longer with the body moving upward, as shown in Fig. 4. Additionally, the liquid column has not broken up and keeps nearly axisymmetric shape in this regime, which are in accord with the

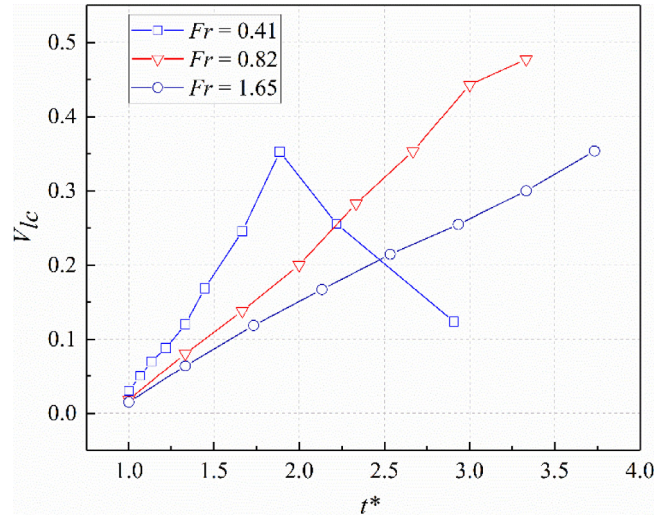


Fig. 7. Temporal evolution of dimensionless liquid column volume pulled out of a liquid pool with different Froude numbers.

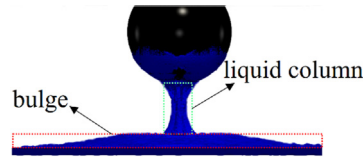


Fig. 8. Schematic diagram of liquid volume pulled out of a liquid pool.

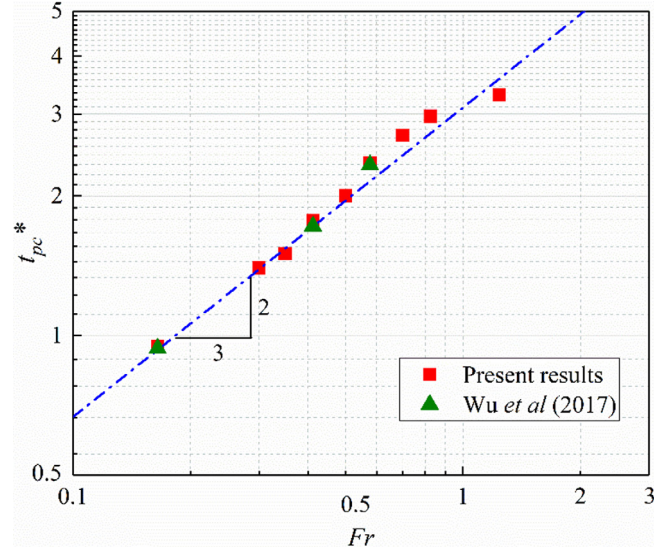


Fig. 9. Pinch-off time as a function of Froude number on a log scale.

experimental results obtained by Reis et al. (2010) and Gart et al. (2015). Besides, the surface curvature of the liquid column depends on both the static contact angle (Guzel and Korkmaz, 2016) and the surface shape of a body initially contacting with the free surface (Gart et al., 2015; Kim et al., 2018; Tassin et al., 2017).

(b) Regime UG (Unstable Growth)

Fig. 10(b) shows that the upper part of the liquid column becomes unstable and asymmetric. Also, its surface deforms irregularly and a few ligaments have been formed before breaking up. Thus, this regime is defined as UG (Unstable

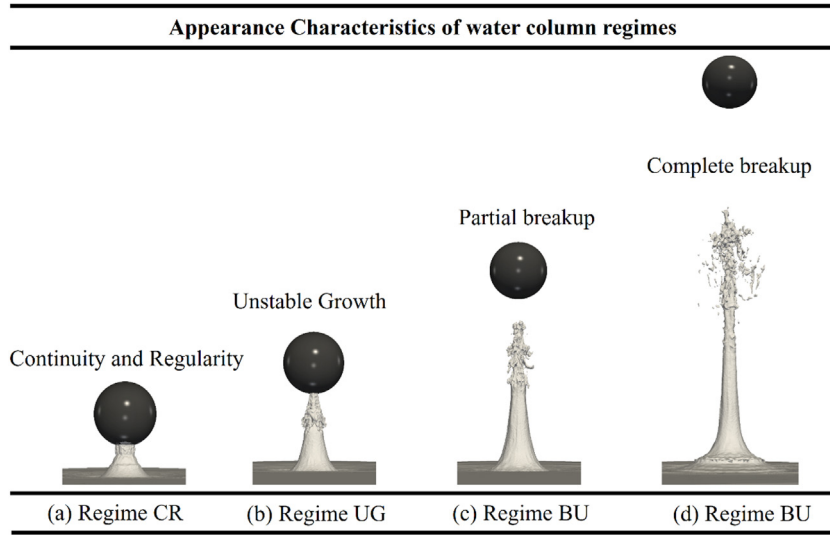


Fig. 10. Three typical liquid column regimes (a) $We = 4690$, $t^* = 1.8$ (b) $We = 75,000$, $t^* = 3.2$ (c) $We = 75,000$, $t^* = 6.4$ (d) $We = 75,000$, $t^* = 14.4$.

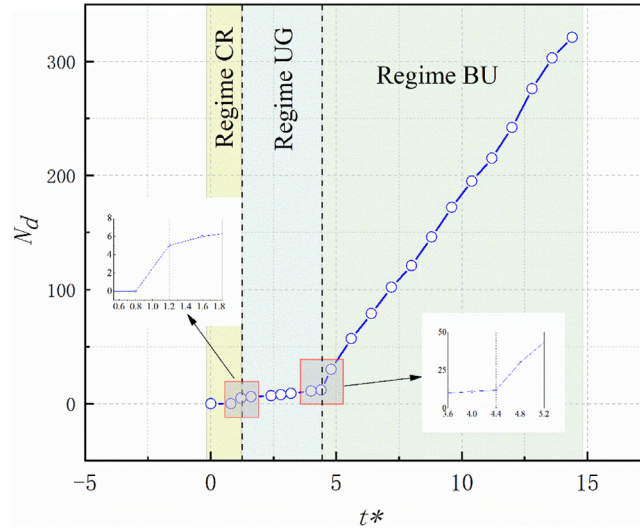


Fig. 11. Time history of the number of ligaments and droplets with a Weber number of 75,000.

Growth). The evolution of the liquid column in regime UG is similar to a round jet. The tip of the liquid column is easily disturbed by the flow field while the root of the liquid column is almost unaffected.

We will take a case about the temporal development of the liquid column shape at $We = 75,000$ as an example to further explain the regime UG, as illustrated in Fig. 12. It can be seen from the region A in Fig. 12(a) that the wave crests occurs primarily in the middle part of liquid column. With the development of the wave crests, it turns into axial direction under the action of gravity. From the region B and C in Fig. 12, the unstable part becomes longer and longer during the sphere moving upward. And, the liquid column near the bottom of the sphere appears unsmooth as well, which indicates that the disturbances are conveyed towards upstream.

This wave on the surface of the liquid column mainly results from the surface instability, which is strongly correlated with its local velocity field, as the strong shear near the liquid surface deforms the liquid surface. Fig. 14 shows contours of instantaneous z -direction velocity. The outer flow velocity is lower than those of the liquid core. Also, the z -direction velocity of outer liquid column is close to zero. Thus, the motion of the crests will be dominated by the gravity. Besides, the disturbances from the moving sphere induce also the surface instability. This disturbance is enhanced with increasing the Weber number.

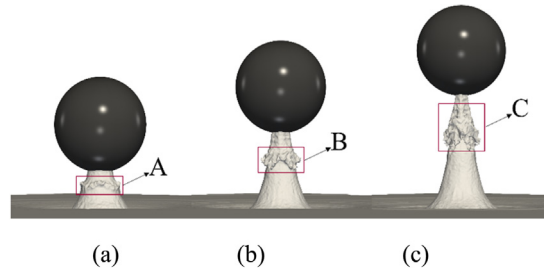


Fig. 12. The development of surface instability of the liquid column in regime UG. The Weber number equals to 75,000. The dimensionless time t^* , (a) $t^* = 1.6$; (b) $t^* = 2.4$; (c) $t^* = 3.2$.

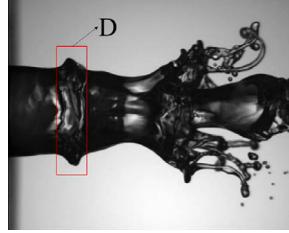


Fig. 13. Development of digitations (Marmottant and Villermaux, 2004b).



Fig. 14. The contours of instantaneous liquid column z -direction velocity in regime UG. The Weber number and Reynolds number equal to 18,712 and 450,000, respectively. The dimensionless time t^* equals to 2. The red line represents the cross section. (For interpretation of the references to colour in this figure legend, the reader is referred to the web version of this article.)

It should be noted that this kind of wave crests at the edge of the liquid column is similar to the experimental results observed by (Marmottant and Villermaux, 2004b), as shown in Fig. 13. They also pointed out the shear instability forms waves on the liquid for the jet. This shear instability consists of the Rayleigh–Taylor (RT) instability and the Kelvin–Helmholtz (KH) instability. However, for the water exit of the sphere, the gas density and velocity are very small in comparison to the water. The gas has little inertia and the strain near the liquid surface is not significant. This is one of the reasons why the liquid–gas two-phase flow is simplified as a single-phase free surface flow in our study. Thus, these two instabilities have little effect on surface instability and deformation of the liquid column. In addition, for the liquid jets in still gases which is similar to the liquid column, Wu et al. (1995) showed that aerodynamic effects at the liquid/gas interface do have a little influence on liquid-phase velocities and turbulence properties prior to breakup.

(c) Regime BU (Breakup)

Fig. 10(c) represents that the liquid column appears to be more unstable and asymmetric than presented in Fig. 10(b). Meanwhile, it is breaking up partially and leads to the formation of some fragments and droplets around its surface. The breakup occurs on the upper part of the liquid column because the liquid near the sphere has higher kinetic energy and velocity than the root of the liquid column. Fig. 10(d) illustrates the upper part of the liquid column completely breaking up. Subsequently, lots of liquid filaments are formed, and then break up into droplets and various liquid packets of different sizes with the stretching of liquid column. These two regimes are defined as BU in consideration of the breakup of liquid column.

The formation of ligaments can be divided into two types. First, some ligaments are formed from the edge of the liquid column due to the surface instability growth. In order to further explain the first stage in the regime BU, the time history of the deformation of the liquid column at $We = 168,750$ and different time scales are displayed, as shown in Fig. 15. It can

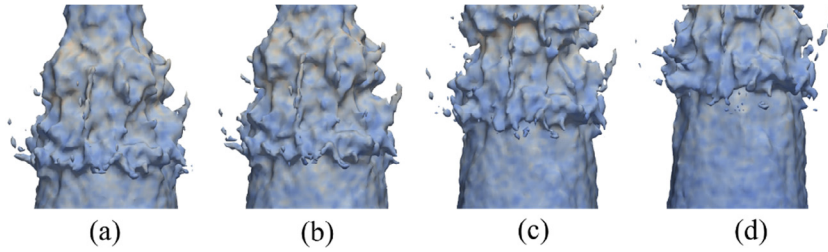


Fig. 15. Instantaneous contours of the liquid surface indicating the breakup of the wave crests into some ligaments and droplets in Regime BU at $We = 168,750$ (a) $t^* = 3.02$, (b) $t^* = 3.30$, (c) $t^* = 3.60$, (d) $t^* = 3.96$.

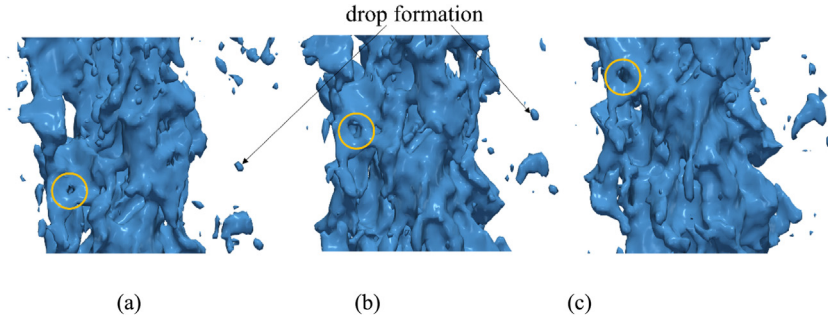


Fig. 16. The intricate forest of ligaments and droplets in completely breakup liquid column at $We = 208,000$ (a) $t^* = 6.0$, (b) $t^* = 6.5$, (c) $t^* = 6.7$.

be seen that the small undulate structures exist on the liquid column surface, i.e. lobes and ligaments. The undulations are not axisymmetric. The crests of the primary transverse modulations are displaced as a whole relative liquid column. These modulations grow in amplitude and eventually degenerate in some liquid ligaments. Moreover, the gravity determines the ligament formation direction and makes ligaments approximately parallel to the z -axis. This kind of breakup at the edge has also occurred in jet experiment observed by [Sallam et al. \(2002\)](#) and numerical simulation of liquid jet obtained by [Shinjo and Umemura \(2010\)](#).

Second, the liquid core disintegrates and forms many ligaments. [Fig. 16](#) shows the intricate forest of ligaments and droplets in regime BU at Weber number = 208,000. The liquid interface is much more disturbed, and more complex breakup can be observed. We can find the hole is created on the liquid column from the yellow circle in [Fig. 16](#). As the time passes, the hole is getting bigger and bigger, and then the disintegration of the liquid core to ligaments occurs.

In addition, most of the liquid energy is supplied as the kinetic energy and potential energy as well as the surface energy which is much lower because the Weber number is too high. As the liquid column rises further upward, the liquid kinetic energy is expected to be transformed into the potential energy. However, the inertial force of the liquid column is still strong due to the unstable disturbance from the sphere. Therefore, the reason why the ligament in the second type is formed and detached from the edge is the liquid inertial force and surface tension force.

Similar to the droplets formation of jet, the detached liquid ligaments with small scales are stretched and their diameter decreases until they break into droplets, as shown in [Fig. 17](#). The capillary waves plays role in the droplet formation. Also, the capillary Plateau-Rayleigh instability determines the ligaments dynamics and the droplet pinch-off dynamics ([Eggers and Villiermaux, 2008](#); [Villiermaux, 2007](#)). There are two modes of pinch-off, i.e., the short-wave mode and the long-wave mode. As shown in [Fig. 17](#), the ligament is short. Thus, only the short-wave mode can exist if any pinch-off of the ligament occurs. And, the ligament breaks up into droplets due to tip contraction and neck development. Furthermore, the main droplet size is strongly correlated to the ligament radius. Because the ligament is variable in size, the sizes of the drops are generally not uniform. Meanwhile, satellite droplets are created. These droplets are smaller than the main ones, as presented in [Fig. 17](#).

5.2. Regime map and transitions

The time scale has an impact on the unstable development and the spatial development of a liquid column, just as it affects the formation of the small structures during jet disintegration. As mentioned above, three regimes have been defined by the deformation of the liquid column lifting from the free surface with different Weber numbers. However, the fundamental question of when a liquid column will become unstable or breakup has not been clearly answered. In an effort to further clarify the deformation of liquid column, we systematically define the regime of the liquid column in the (We, t^*) plane over a wide range of Weber number ($520 \leq We \leq 210,000$) and non-dimensional time $t^* \leq 12.5$.

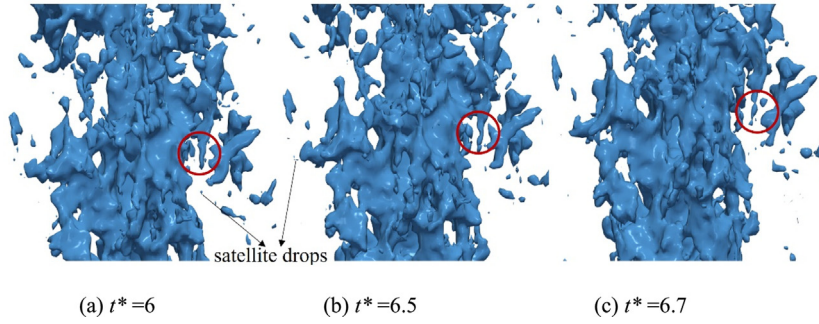


Fig. 17. Droplet formation from the ligament at $We = 208,000$.

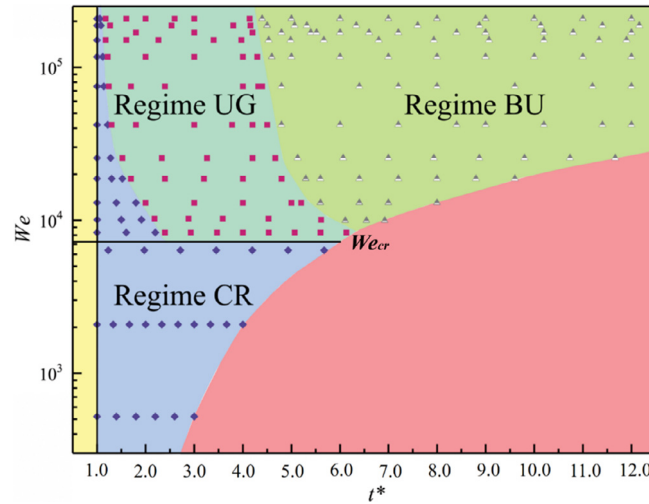


Fig. 18. Map of regimes of the liquid column in the $\{We, t^*\}$ plane.

Fig. 18 shows the map of regimes of the liquid column in the $\{We, t^*\}$ plane. The blue rhombus corresponds to the 'CR' regime, where the shape of the liquid column is regular during its extension. Despite previous reports of the regular and steady liquid column [e.g., Gart et al. (2015) and Wu et al. (2017)], no spheres within the range of parameters is studied in this map. The red solid blocks correspond to the 'UG' regime, in which the waves on the surface of the liquid column develop due to the surface instability. Also, the triangles correspond to the 'BU' regime, where the breakup of the liquid column occurs.

At $t^* = 1$, the bottom of the sphere reaches the undisturbed free surface. Consequently, the liquid column has not been formed before this moment. Besides, the red area in Fig. 18 has not been discussed because the liquid column begins to descend after pinch-off. It should be mentioned that we focus on the rising process of the liquid column. The falling liquid column will be considered in future studies.

As seen in Fig. 18, the liquid column stays in the regime CR and does not undergo the transition from the regime CR to regime UG at We less than 7500. At this range, the character of the shape of the liquid column becomes dependent on Weber number. The time scales have no effect on the development of the surface instability. Besides, the present map shows a distinct boundary line between the regime CR and the regime UG when the non-dimensional time t^* is greater than 2.4. This black line indicates that the critical Weber number (We_{cr}) is almost constant over the wide ranges of time scales and its value approximately equals 7000. It should be emphasized that the non-dimensional time for the transition from the regime CR to the regime UG is reduced as the Weber number increases when the non-dimensional time t^* is less than 2.4.

It can be clearly found in Fig. 18 that the regime UG and regime BU become the main mode for the liquid column. The unstable part of the liquid column occurs at the moment when the sphere rises a short distance at Weber number above 7500. Additionally, the higher the Weber number is, the shorter time the transition from the regime UG to the regime BU experiences. The reason may be that the initial disturbance from the sphere is enhanced with increasing its Weber number.

Besides, these transitions in regimes are associated with a distinct change in the velocity field of the liquid column, which results from the Reynolds number increasing as the sphere velocity increases. Fig. 19 shows the contours of

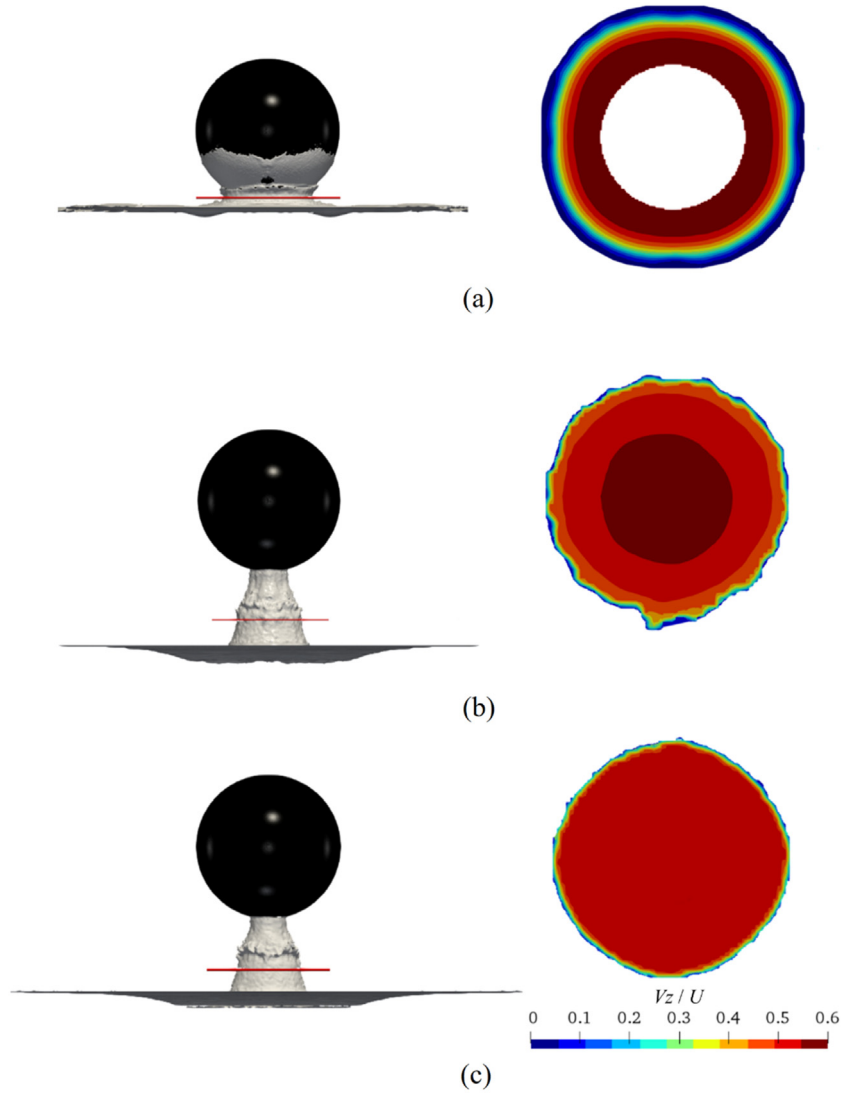


Fig. 19. Contours of instantaneous liquid column z -direction velocity in regime UG (a) $We=520$, $Re=75,000$; (b) $We=33,266$, $Re=60,000$; (c) $We=208,000$, $Re=150,000$.

instantaneous liquid column axial velocity in regime UG with different Weber numbers and Reynolds numbers. The white region inside the cross section in Fig. 19(a) denotes the section of the sphere. It can be clearly seen that the z -direction velocity gradient in the liquid column boundary for the transverse direction increases with increasing the Reynolds numbers, which results from the increase in the velocity of the sphere that excites the unstable disturbances at the liquid column surface. Finally, it leads to the increase in shear instability in the surface of the liquid column. Thus, the breakup of the liquid column occurs more easily for high Reynolds number.

6. Conclusion

In this paper, nonlinear deformation and breakup of the liquid column pulled by a partially submerged sphere are investigated with different parameters, namely Froude number, Weber number, time scales. The three-dimensional model of water exit has been established on the basis of the Lattice Boltzmann method. The three-dimensional water exit of a partially submerged sphere with constant vertical velocity is simulated, which are validated with the experimental results of Song et al. (2019). We have got a good agreement with the experimental results regarding the deformation of the free surface. The effectiveness of this approach is well verified.

The dynamic deformation of the liquid column is studied before its breakup. The liquid column shape exhibits a cone-like structure due to the inertia effect during the sphere moving upward. The upper portion of the liquid column contracts,

whereas the expansion of its bottom occurs, which is confirmed by the radial velocity of the liquid column. As the Froude number increases, the dimensionless liquid column volume dramatically decreases because of the formation of the bugle near free surface. In addition, the power law $t_{pc}^{**} \sim Fr^{2/3}$ is obtained for the pinch-off time and the Froude number.

The breakup of the liquid column depends on the Weber number and the time scales. The deformation of the liquid column has been divided into different regimes that reflects differences in the number of ligaments and droplets as the conditions are changed. The regimes include the regime CR, the regime UG and the regime BU. For the regime CR, the liquid column keeps nearly axisymmetric shape all the time during its stretching. As the Weber number increases to the critical Weber number that approximately equals 7000, the appearance of the liquid column becomes irregular and unstable in the regime UG, which results from its velocity gradient and the disturbance from the sphere. Besides, our computations predict the smaller structures on the liquid column surface in this regime, i.e. lobes, bridges and ligaments, which are the precursors to droplet.

As the time scale advances, many ligaments are formed at the regime BU. The formation of ligaments can be divided into two types. First, some ligaments are formed from the edge of the liquid column due to the surface instability. Second, many ligaments are formed from the disintegration of liquid core under the action of gravity and inertia. The ligament direction is determined by the gravity and parallel to the z -axis. Then, the ligaments break up into the droplets due to the capillary Plateau-Rayleigh instability. The size of droplets is strongly correlated to the ligament radius.

Our present studies are limited to the stretching of the liquid column during the rising process of a sphere. Therefore, our future work will include the evolution of the liquid column during its downward descent. Additionally, the effect of the contact angle of the sphere on deformation of the liquid column is investigated systematically in the future.

Declaration of competing interest

The authors declare that they have no known competing financial interests or personal relationships that could have appeared to influence the work reported in this paper.

Acknowledgment

We would like to thank the Chinese Scholarship Council and the National Natural Science Foundation of China (52006045) for its financial support. We also thank the referees whose comments have improved the quality of the paper.

References

- Amirshaghagh, H., Rahimian, M.H., Safari, H., Krafczyk, M., 2018. Large eddy simulation of liquid sheet breakup using a two-phase lattice Boltzmann method. *Comput. Fluids* 160, 93–107. <http://dx.doi.org/10.1016/j.compfluid.2017.10.023>.
- Benzi, R., Succi, S., Vergassola, M., 1992. The lattice Boltzmann equation: theory and applications. *Phys. Rep.* 222, 145–197. [http://dx.doi.org/10.1016/0370-1573\(92\)90090-M](http://dx.doi.org/10.1016/0370-1573(92)90090-M).
- Biscarini, C., Di Francesco, S., Nardi, F., Manciola, P., 2013. Detailed simulation of complex hydraulic problems with macroscopic and mesoscopic mathematical methods. *Math. Prob. Eng.* 2013, <http://dx.doi.org/10.1155/2013/928309>.
- Buick, J.M., Greated, C.A., 2000. Gravity in a lattice Boltzmann model. *Phys. Rev. E* 61, 5307–5320. <http://dx.doi.org/10.1103/PhysRevE.61.5307>.
- Champougny, L., Rio, E., Restagno, F., Scheid, B., 2017. The break-up of free films pulled out of a pure liquid bath. *J. Fluid Mech.* 811, 499–524. <http://dx.doi.org/10.1017/jfm.2016.758>.
- Chang, B., Myeong, J., Viro, E., Clanet, C., Kim, H.-Y., Jung, S., 2019. Jumping dynamics of aquatic animals. *J. R. Soc. Interface* 16, 20190014. <http://dx.doi.org/10.1098/rsif.2019.0014>.
- Chen, S., Chen, H., Martinez, D., Matthaeus, W., 1991. Lattice Boltzmann model for simulation of magnetohydrodynamics. *Phys. Rev. Lett.* 67, 3776–3779. <http://dx.doi.org/10.1103/PhysRevLett.67.3776>.
- Chen, S., Doolen, G.D., 1998. Lattice Boltzmann method for fluid flows. *Annu. Rev. Fluid Mech.* 30, 329–364. <http://dx.doi.org/10.1146/annurev.fluid.30.1.329>.
- Chen, Y., Wang, H., Helbling, E.F., Jafferis, N.T., Zufferey, R., Ong, A., Ma, K., Gravish, N., Chirarattananon, P., Kovac, M., Wood, R.J., 2017. A biologically inspired, flapping-wing, hybrid aerial-aquatic microrobot. *Sci. Robot.* 2, eaao5619. <http://dx.doi.org/10.1126/scirobotics.aao5619>.
- Dodds, S., Carvalho, M.D. S., Kumar, S., 2009. Stretching and slipping of liquid bridges near plates and cavities. *Phys. Fluids* 21, 092103. <http://dx.doi.org/10.1063/1.3212963>.
- Dodds, S., Carvalho, M.S., Kumar, S., 2012. The dynamics of three-dimensional liquid bridges with pinned and moving contact lines. *J. Fluid Mech.* 707, 521–540. <http://dx.doi.org/10.1017/jfm.2012.296>.
- Doshi, P., Cohen, I., Zhang, W.W., Siegel, M., Howell, P., Basaran, O.A., Nagel, S.R., 2003. Persistence of memory in drop breakup: The breakdown of universality. *Science* (80-) 302, 1185. <http://dx.doi.org/10.1126/science.1089272>.
- Ducros, F., Nicoud, F., Poinsot, T., 1998. Wall-adapting local eddy-viscosity models for simulations in complex geometries. In: *Numerical Methods for Fluid Dynamics VI*. pp. 293–299.
- Eggers, J., 1997. Nonlinear dynamics and breakup of free-surface flows. *Rev. Mod. Phys.* 69, 865–930. <http://dx.doi.org/10.1103/RevModPhys.69.865>.
- Eggers, J., Villiermaux, E., 2008. Physics of liquid jets. *Rep. Prog. Phys.* 71, 036601. <http://dx.doi.org/10.1088/0034-4885/71/3/036601>.
- Facci, A.L., Falcucci, G., Agresta, A., Biscarini, C., Jannelli, E., Ubertini, S.J.W., 2019. Fluid structure interaction of buoyant bodies with free surface flows: Computational modelling and experimental validation. 11, 1048. <http://dx.doi.org/10.3390/w11051048>.
- Falcucci, G., Ubertini, S., Bella, G., De Maio, A., Palpacelli, S., 2010. Lattice Boltzmann modeling of diesel spray formation and break-up. *SAE Int. J. Fuels Lubr.* 3, 582–593.
- Falcucci, G., Ubertini, S., Biscarini, C., Francesco, S.D., Chiappini, D., Palpacelli, S., Maio, A.D., Succi, S., 2011. Lattice Boltzmann methods for multiphase flow simulations across scales. *Commun. Comput. Phys.* 9, 269–296. <http://dx.doi.org/10.4208/cicp.221209.250510a>.
- Faltinsen, O., 1993. *Sea Loads on Ships and Offshore Structures*. Cambridge University Press.
- Filippova, O., Hänel, D., 1997. Lattice-Boltzmann simulation of gas-particle flow in filters. *Comput. Fluids* 26, 697–712. [http://dx.doi.org/10.1016/S0045-7930\(97\)00009-1](http://dx.doi.org/10.1016/S0045-7930(97)00009-1).

- Gart, S., Socha, J.J., Vlachos, P.P., Jung, S., 2015. Dogs lap using acceleration-driven open pumping. *Proc. Natl. Acad. Sci. U.S.A.* 112 (15798), <http://dx.doi.org/10.1073/pnas.1514842112>.
- Greenhow, M., Lin, W.-M., 1983. *Nonlinear-Free Surface Effects: Experiments and Theory*. Massachusetts Inst Of Tech Cambridge Dept Of Ocean Engineering.
- Gunstensen, A.K., Rothman, D.H., Zaleski, S., Zanetti, G., 1991. Lattice Boltzmann model of immiscible fluids. *Phys. Rev. A* 43, 4320–4327. <http://dx.doi.org/10.1103/PhysRevA.43.4320>.
- Guo, C., Liu, T., Hao, H., Chang, X., 2019. Evolution of water column pulled by partially submerged spheres with different velocities and submergence depths. *Ocean Eng.* 187, 106087. <http://dx.doi.org/10.1016/j.oceaneng.2019.05.069>.
- Guzel, B., Korkmaz, F.C., 2016. Experimental investigation of water exit under hydrophobic effects. In: *ASME 2016 35th International Conference on Ocean, Offshore and Arctic Engineering*. <http://dx.doi.org/10.1115/OMAE2016-54636>.
- Hao, H., Song, Y., Yu, J., Chen, F., Liu, T., 2019. Numerical analysis of water exit for a sphere with constant velocity using the lattice Boltzmann method. *Appl. Ocean Res.* 84, 163–178. <http://dx.doi.org/10.1016/j.apor.2018.12.010>.
- Hou, S., Sterling, J., Chen, S., Doolen, G., 1994. A lattice Boltzmann subgrid model for high Reynolds number flows. *arXiv preprint comp-gas/9401004*. <https://arxiv.org/abs/comp-gas/9401004>.
- Jarrahbashi, D., Sirignano, W.A., Popov, P.P., Hussain, F., 2016. Early spray development at high gas density: hole, ligament and bridge formations. *J. Fluid Mech.* 792, 186–231. <http://dx.doi.org/10.1017/jfm.2016.71>.
- Kékesi, T., Amberg, G., Prahl Wittberg, L., 2014. Drop deformation and breakup. *Int. J. Multiph. Flow.* 66, 1–10. <http://dx.doi.org/10.1016/j.ijmultiphaseflow.2014.06.006>.
- Kim, W., Bush, J.W.M., 2012. Natural drinking strategies. *J. Fluid Mech.* 705, 7–25. <http://dx.doi.org/10.1017/jfm.2012.122>.
- Kim, S.J., Kim, S., Jung, S., 2018. Extremes of the pinch-off location and time in a liquid column by an accelerating solid sphere. *Phys. Rev. Fluids* 3, 084001. <http://dx.doi.org/10.1103/PhysRevFluids.3.084001>.
- Komrakova, A.E., Shardt, O., Eskin, D., Derksen, J.J., 2014. Lattice Boltzmann simulations of drop deformation and breakup in shear flow. *Int. J. Multiph. Flow.* 59, 24–43. <http://dx.doi.org/10.1016/j.ijmultiphaseflow.2013.10.009>.
- Körner, C., Thies, M., Hofmann, T., Thürey, N., Rüde, U., 2005. Lattice Boltzmann model for free surface flow for modeling foaming. *J. Stat. Phys.* 121, 179–196. <http://dx.doi.org/10.1007/s10955-005-8879-8>.
- Krüger, T., Kusumaatmaja, H., Kuzmin, A., Shardt, O., Silva, G., Viggen, E.M., 2016. *The Lattice Boltzmann Method: Principles and Practice*. Springer, Berlin, Germany.
- Liju, P.Y., Machane, R., Cartellier, A., 2001. Surge effect during the water exit of an axisymmetric body traveling normal to a plane interface: experiments and BEM simulation. *Exp. Fluids* 31, 241–248. <http://dx.doi.org/10.1007/s003480100277>.
- Marmottant, P., Villermaux, E., 2004a. Fragmentation of stretched liquid ligaments. *Phys. Fluids* 16, 2732–2741. <http://dx.doi.org/10.1063/1.1756030>.
- Marmottant, P., Villermaux, E., 2004b. On spray formation. *J. Fluid Mech.* 498, 73–111. <http://dx.doi.org/10.1017/S0022112003006529>.
- Mei, R., Shyy, W., Yu, D., Luo, L.-S., 2000. Lattice Boltzmann method for 3-D flows with curved boundary. *J. Comput. Phys.* 161, 680–699. <http://dx.doi.org/10.1006/jcph.2000.6522>.
- Mei, R., Yu, D., Shyy, W., Luo, L.-S., 2002. Force evaluation in the lattice Boltzmann method involving curved geometry. *Phys. Rev. E* 65, 041203. <http://dx.doi.org/10.1103/PhysRevE.65.041203>.
- Mitchell, T., Leonardi, C., Fakhari, A., 2018. Development of a three-dimensional phase-field lattice Boltzmann method for the study of immiscible fluids at high density ratios. *Int. J. Multiph. Flow.* 107, 1–15. <http://dx.doi.org/10.1016/j.ijmultiphaseflow.2018.05.004>.
- Ni, B.Y., Zhang, A.M., Wu, G.X., 2015. Simulation of complete water exit of a fully-submerged body. *J. Fluids Struct.* 58, 79–98. <http://dx.doi.org/10.1016/j.jfluidstructs.2015.07.010>.
- Qian, Y.H., D'Humières, D., Lallemand, P., 1992. Lattice BGK models for Navier–Stokes equation. *Europhys. Lett.* 17, 479–484. <http://dx.doi.org/10.1209/0295-5075/17/6/001>.
- Rajavaheanthan, R., Greenhow, M., 2015. Constant acceleration exit of two-dimensional free-surface-piercing bodies. *Appl. Ocean Res.* 50, 30–46. <http://dx.doi.org/10.1016/j.apor.2014.07.007>.
- Reis, P.M., Jung, S., Aristoff, J.M., Stocker, R., 2010. How cats lap: Water uptake by felis catus. *Science* 330, 1231–1234. <http://dx.doi.org/10.1126/science.1195421>.
- Russo, S., Biscarini, C., Facci, A.L., Falcucci, G., Jannelli, E., Ubertini, S., 2018a. Experimental assessment of buoyant cylinder impacts through high-speed image acquisition. *J. Mar. Sci. Technol.* 23, 67–80. <http://dx.doi.org/10.1007/s00773-017-0456-8>.
- Russo, S., Jalalilendi, M., Falcucci, G., Porfiri, M., 2018b. Experimental characterization of oblique and asymmetric water entry. *Exp. Therm Fluid Sci.* 92, 141–161. <http://dx.doi.org/10.1016/j.expthermflusci.2017.10.028>.
- Sallam, K.A., Dai, Z., Faeth, G.M., 2002. Liquid breakup at the surface of turbulent round liquid jets in still gases. *Int. J. Multiph. Flow.* 28, 427–449. [http://dx.doi.org/10.1016/S0301-9322\(01\)00067-2](http://dx.doi.org/10.1016/S0301-9322(01)00067-2).
- Shinjo, J., Umehura, A., 2010. Simulation of liquid jet primary breakup: Dynamics of ligament and droplet formation. *Int. J. Multiph. Flow.* 36, 513–532. <http://dx.doi.org/10.1016/j.ijmultiphaseflow.2010.03.008>.
- Song, X., Wu, Q.G., Ni, B.Y., Chen, H.L., 2019. Deformation and bubble entrapment of free surface before axisymmetric bodies detaching from water fully. *J. Mech.* 35, 863–874. <http://dx.doi.org/10.1017/jmech.2018.62>.
- Sukop, M., Thorne Jr, D., 2006. *Lattice Boltzmann Modeling*, first ed.
- Tassin, A., Breton, T., Forest, B., Ohana, J., Chalony, S., Le Roux, D., Tancray, A., 2017. Visualization of the contact line during the water exit of flat plates. *Exp. Fluids* 58 (104), <http://dx.doi.org/10.1007/s00348-017-2383-1>.
- Tassin, A., Piro, D.J., Korobkin, A.A., Maki, K.J., Cooker, M.J., 2013. Two-dimensional water entry and exit of a body whose shape varies in time. *J. Fluids Struct.* 40, 317–336. <http://dx.doi.org/10.1016/j.jfluidstructs.2013.05.002>.
- Thürey, N., 2007. *Physically based animation of free surface flows with the lattice Boltzmann method*. University of Erlangen.
- Villermaux, E., 2007. Fragmentation. *Annu. Rev. Fluid Mech.* 39, 419–446. <http://dx.doi.org/10.1146/annurev.fluid.39.050905.110214>.
- Wang, Y., Liao, L., Du, T., Huang, C., Liu, Y., Fang, X., Liang, N., 2014. A study on the collapse of cavitation bubbles surrounding the underwater-launched projectile and its fluid–structure coupling effects. *Ocean Eng.* 84, 228–236. <http://dx.doi.org/10.1016/j.oceaneng.2014.04.014>.
- Weickgenannt, C., Roisman, I.V., Tropea, C., 2015. Pinch-off of a stretching viscous filament and drop transport. *New J. Phys.* 17, 083059. <http://dx.doi.org/10.1088/1367-2630/17/8/083059>.
- Wu, P., Hsiang, L., Faeth, G., 1995. Aerodynamic effects on primary and secondary spray breakup. In: *J Liquid Rocket Engine Combustion Instability*. American Institute of Aeronautics Astronautics, Inc, Washington, DC, pp. 247–279.
- Wu, Q.G., Ni, B.Y., Bai, X.L., Cui, B., Sun, S.L., 2017. Experimental study on large deformation of free surface during water exit of a sphere. *Ocean Eng.* 140, 369–376. <http://dx.doi.org/10.1016/j.oceaneng.2017.06.009>.
- Xing, X.Q., Butler, D.L., Ng, S.H., Wang, Z., Danyluk, S., Yang, C., 2007. Simulation of droplet formation and coalescence using lattice Boltzmann-based single-phase model. *J. Colloid Interface Sci.* 311, 609–618. <http://dx.doi.org/10.1016/j.jcis.2007.02.088>.
- Zarghami, A., Falcucci, G., Jannelli, E., Succì, S., Porfiri, M., Ubertini, S., 2014. Lattice Boltzmann modeling of water entry problems. *Internat. J. Modern Phys. C* 25, 1441012. <http://dx.doi.org/10.1142/S0129183114410125>.

- Zhang, X., Padgett, R.S., Basaran, O.A., 1996. Nonlinear deformation and breakup of stretching liquid bridges. *J. Fluid Mech.* 329, 207–245. <http://dx.doi.org/10.1017/S0022112096008907>.
- Zhu, X., Faltinsen, O.M., Hu, C., 2006. Water entry and exit of a horizontal circular cylinder. *J. Offshore Mech. Arct. Eng.* 129, 253–264. <http://dx.doi.org/10.1115/1.2199558>.
- Zhuang, J., Ju, Y.S., 2015. A combined experimental and numerical modeling study of the deformation and rupture of axisymmetric liquid bridges under coaxial stretching. *Langmuir* 31, 10173–10182. <http://dx.doi.org/10.1021/acs.langmuir.5b02102>.